Article

Magnetic Photocatalyst BiVO$_4$/Mn-Zn ferrite/Reduced Graphene Oxide: Synthesis Strategy and Its Highly Photocatalytic Activity

Taiping Xie [1,2] , Hui Li [3], Chenglun Liu [1,3,*], Jun Yang [4], Tiancun Xiao [5] and Longjun Xu [1,*]

[1] State Key Laboratory of Coal Mine Disaster Dynamics and Control, Chongqing University, Chongqing 400044, China; deartaiping@163.com

[2] Chongqing Key Laboratory of Extraordinary Bond Engineering and Advanced Materials Technology (EBEAM), Yangtze Normal University, Chongqing 408100, China

[3] College of Chemistry and Chemical Engineering, Chongqing University, Chongqing 401331, China; lihui@163.com

[4] Chongqing Key Laboratory of Environmental Materials & Remediation Technologies Chongqing University of Arts and Sciences, Yongchuan 402160, China; yangjun@163.com

[5] Inorganic Chemistry Laboratory, University of Oxford, Oxford OX1 3QR, UK; xiaotiancun@chem.ox.ac.uk

* Correspondence: xlclj@cqu.edu.cn (C.L.); xulj@cqu.edu.cn (L.X.); Tel.: +86-138-8370-2103 (C.L.); +86-153-1060-6337 (L.X.)

check for updates

Abstract: Magnetic photocatalyst BiVO$_4$/Mn-Zn ferrite (Mn$_{1-x}$Zn$_x$Fe$_2$O$_4$)/reduced graphene oxide (RGO) was synthesized by a simple calcination and reduction method. The magnetic photocatalyst held high visible light-absorption ability with low band gap energy and wide absorption wavelength range. Electrochemical impedance spectroscopies illustrated good electrical conductivity which indicated low charge-transfer resistance due to incorporation of Mn$_{1-x}$Zn$_x$Fe$_2$O$_4$ and RGO. The test of photocatalytic activity showed that the degradation ratio of rhodamine B (RhB) reached 96.0% under visible light irradiation after only 1.5 h reaction. The photocatalytic mechanism for the prepared photocatalyst was explained in detail. Here, the incorporation of RGO enhanced the specific surface area compared with BiVO4/Mn$_{1-x}$Zn$_x$Fe$_2$O$_4$. The larger specific surface area provided more active surface sites, more free space to improve the mobility of photo-induced electrons, and further facilitated the effective migration of charge carriers, leading to the remarkable improvement of photocatalytic performance. Meanwhile, RGO was the effective acceptor as well as transporter of photo-generated electron hole pairs. $\bullet O_2^-$ was the most active species in the photocatalytic reaction. BiVO$_4$/Mn$_{1-x}$Zn$_x$Fe$_2$O$_4$/RGO had quite a wide application in organic contaminants removal or environmental pollution control.

Keywords: BiVO$_4$; RGO; Mn–Zn ferrite; magnetic photocatalyst; magnetic performance; photocatalytic mechanism

1. Introduction

In the recent decade, composite semiconductor materials are considered extraordinarily attractive in the field of solar energy and pollution control engineering. Many kinds of photocatalytic composite materials with superior optical properties and high photo-induced activity have been synthesized and studied [1,2]. However, the utilization efficiency of visible light for some photocatalysts is very low, owing to their large intrinsic band gap energy, which impels scientists to explore new photocatalytic compounds with high visible light-driven photocatalytic activity. Bismuth-based composites with *n*-type junctions exhibited excellent photocatalytic activity and high stability [3]. Among them,

monoclinic crystal $BiVO_4$, due to its relatively lower band gap energy has been of much interest in the photocatalysis field. Nevertheless, single component $BiVO_4$ has poor absorption ability for visible light, leading to low quantum efficiency.

Meanwhile, the difficulty in separation and recovery for bismuth-contained photocatalysts greatly restricts their industrial application. Therefore, magnetic composite photocatalysts are vitally important in photocatalysis materials science, due to their simple recovery via an external magnet after reaction. Magnetic compounds, such as Fe_3O_4 and $ZnFe_2O_4$, have been extensively studied, due to their interesting properties, including photoactivity and stability. There are synthesis strategies and property studies for magnetic composite catalysts [4–8]. However, the recovery rate and the photocatalytic activity of these composites do not meet the need of industrial applications yet. Comparing magnetization and stability, $Mn_{1-x}Zn_xFe_2O_4$ is superior to Fe_3O_4 and $ZnFe_2O_4$.

Reduced graphene oxide (RGO) possessing several good properties (e.g., electrical conductivity, optical transparency and carrier mobility) has been paid considerable attention [9–11]. Single layer graphene sheet is composed of sp^2-hybridized carbon atoms in the two-dimension honeycomb lattice, which donates high mobility for electron carriers. The distinctive structure of RGO determines that its band gap energy is zero [12,13]. There are reports on the preparation method for RGO-composed catalysts and their activity [14–16]. It is reasonable to mingle RGO with $BiVO_4$, which is aimed at enhancement of the migration rate of photo-produced electrons and holes of $BiVO_4$. Previous investigation showed that $BiVO_4$–RGO composite possessed photocatalytic performance and redox ability [17]. Unexpectedly, a larger visible light photocatalytic activity could not be observed in $BiVO_4$–RGO system under visible light irradiation [18,19].

Here, fabrication of $BiVO_4/Mn_{1-x}Zn_xFe_2O_4/RGO$ was a continuation of our research about the syntheses and application of $BiVO_4/Mn_{1-x}Zn_xFe_2O_4$ [20]. The RhB degradation reaction using $BiVO_4/Mn_{1-x}Zn_xFe_2O_4$ as photocatalyst was slow (take 3 h). The incorporation of RGO could boost the photocatalytic reaction kinetics. Here, the photocatalytic activity and mechanism are deeply investigated with RhB degradation and the radical capturing experiments using $BiVO_4/Mn_{1-x}Zn_xFe_2O_4/RGO$ as photocatalyst.

2. Experimental Procedures

2.1. Preparation of BiVO₄/Mn₁₋ₓZnₓFe₂O₄/RGO

$BiVO_4/Mn_{1-x}Zn_xFe_2O_4$ was prepared according to our previous report [20]. Graphene oxide (GO) was fabricated with improving Hummars method [21].

GO (36.0 mg) and 1.2 g $BiVO_4/Mn_{1-x}Zn_xFe_2O_4$ were dispersed in deionized water with ultrasonication and stirring for 2 h. GO was reduced into RGO with NH_3 H_2O–N_2H_4 H_2O solution (1.0 mL–3.0 mL), then filtered and washed four times with deionized water and ethanol before placing at 80 °C for 2 h. $BiVO_4/Mn_{1-x}Zn_xFe_2O_4/RGO$ was obtained after drying at 60 °C for 24 h.

2.2. Materials Characterization

The phase and structure of samples were determined by X-ray Diffractometer (Shimadzu, XRD-6000, Kyoto, Japan), Fourier transform infrared spectroscopy (FTIR, Perkin-Elmersystem 2000, Akron, OH, USA), and INVIA Raman microprobe (Renishaw Instruments, Wotton-under-Edge, UK). The light absorption, magnetization, and surface performances of samples were examined by ultraviolet–visible diffuse reflectance spectrophotometer (UV–vis DRS, TU1901, Beijing, China), vibrating sample magnetometer (VSM 7410, LakeShore, Carson, CA, USA), Brunauer–Emmett–Teller (BET, ASAP-2020, Micromeritics, Norcross, GA, USA). The electrochemical workstation (PGSTAT30) was employed to measure electrochemical impedance spectroscopy (EIS) of the as-prepared samples. The test parameters of EIS were the following, $K_3[Fe(CN)_6]/K_4[Fe(CN)_6]$ (1:1)—KCl electrolyte solution was employed. The work electrode content contained the as-produced catalyst, acetylene black, and polytetrafluoroethylene (mass ratio, 85.0:10:5), the counter electrode was platinum foils, and the

reference electrode was the saturated calomel electrode (SCE), setting AC voltage amplitude of 5 mV and a frequency range of 1×10^5–1×10^{-2} Hz.

2.3. Photocatalytic Activity, Stability, and Corresponding Mechanism

The photocatalytic activity of $BiVO_4/Mn_{1-x}Zn_xFe_2O_4/RGO$ was investigated by the rhodamine B (RhB) degradation under visible light irradiation [22]. Ninety milligrams of composite photocatalyst (named fresh photocatalyst) was put into 5.0 mg/L RhB solution (100.0 mL). The solution was placed for 0.5 h with stirring in the dark to reach the adsorption–desorption equilibrium. A 500 W Xe lamp was used as the visible light source, equipped with ultraviolet (UV) light cut-off filter ($\lambda \geq 400$ nm). At given irradiation time intervals, a series of the reaction solution was sampled and the absorption spectrum was measured.

The stability for the photocatalyst were assessed by cycling tests. After each cycle, the photocatalyst was separated and recovered by means of an external magnet. The recovered catalyst was respectively washed with ethanol and deionized water, then dried at the end of each cycle.

The photocatalytic mechanism of $BiVO_4/Mn_{1-x}Zn_xFe_2O_4/RGO$ was explored by holes-radical trapping experiments with *p*-benzoquinone (BZQ,) (•O_2^- radical scavenger), Na_2-EDTA (hole scavenger), and *tert*-butanol (*t*-BuOH) (•OH radical scavenger) in photocatalytic reaction.

3. Results and Discussion

3.1. Optimal Synthesis Condition

The $Mn_{1-x}Zn_xFe_2O_4$, prepared in advance, had a strong magnetization. In order to completely form $BiVO_4$ precursor and reduce the impurity, $Mn_{1-x}Zn_xFe_2O_4$ was put into the precursor instead of $Bi(NO_3)_3$ solution, in other words, $BiVO_4$ precursor was already formed before magnetic substance was added. $Mn_{1-x}Zn_xFe_2O_4/BiVO_4$ was assembled via calcination at only 450 °C. This temperature was lower than that of $Mn_{1-x}Zn_xFe_2O_4$ formation (1200 °C), as well as $BiVO_4$ formation (500 °C). Therefore, the calcination approach was indeed low-cost and economical.

GO was dispersed in $BiVO_4/Mn_{1-x}Zn_xFe_2O_4$ with deionized water under room temperature, RGO was produced by $NH_3 H_2O + N_2H_4 H_2O$ reduction of GO without heating. This in situ synthesis method was simple and with low-energy consumption.

3.2. Structure and Phase Identification

The XRD spectra of the obtained samples were shown in Figure 1. The characteristic spectra (Figure 1b–d) of monoclinic crystal $BiVO_4$ was well indexed with the standard card (JCPDS card No: 14-0688) [17], corresponding to the diffraction phases of (110), (011), (121), (040), (200), (002), (211), (150), (132), and (042). The diffraction pattern in Figure 1a of $Mn_{1-x}Zn_xFe_2O_4$ was fully matched with the standard card (JCPDS card No: 74-2400), agreeing with the result of the literature report [20]. The diffraction peaks of $Mn_{1-x}Zn_xFe_2O_4$ patterns were hardly observed in Figure 1c,d. Not only was the amount (15.0%) of the magnetic matrix low, but also, the diffraction patterns location of $Mn_{1-x}Zn_xFe_2O_4$ overlapped with the domain diffraction patterns of $BiVO_4$. The diffraction peak of GO (Figure 1e) was observed at 10.8° (crystal plane (001)) [23]. However, the peak (Figure 1d) disappeared after GO was mostly reduced to RGO under the reduction of $NH_3 H_2O$ and $N_2H_4 H_2O$ [24]. Moreover, the amount (3%, *w/w*) of RGO was not enough to be detected in X-ray diffraction. In short, it was deduced that the prepared samples totally exhibited good crystallinity.

The peak–intensity ratio (I_D/I_G) of D band (~1364.0 cm^{-1}, originating from disorder-activated Raman mode) and G band (~1598.0 cm^{-1}, corresponding to sp^2 hybridized carbon) in RGO was usually used to assess the reduction extent. Figure 2 showed the Raman spectra of the above-obtained samples. It was seen that G-band of RGO was shifted from 1598.0 cm^{-1} to 1589.0 cm^{-1}, while the D-band shorted from 1364.0 cm^{-1} to 1352 cm^{-1} after the thermal reduction finished. The I_D/I_G ratio of GO was 1.10, and that of $BiVO_4/Mn_{1-x}Zn_xFe_2O_4/RGO$ decreased to 0.84. The relative low I_D/I_G

ratio of RGO implied high reduction efficiency in $BiVO_4/Mn_{1-x}Zn_xFe_2O_4/RGO$ [17]. Typical Raman bands of $BiVO_4$ were located at 120.0, 210.0, 324.0, 366.0, and 826.0 cm^{-1} in Figure 2. The two bands at 324.0 cm^{-1} and 366.0 cm^{-1} changed into one wide band in $BiVO_4/Mn_{1-x}Zn_xFe_2O_4$, as well as in $BiVO_4/Mn_{1-x}Zn_xFe_2O_4/RGO$. The result was also consistent with the results of the previous report [25].
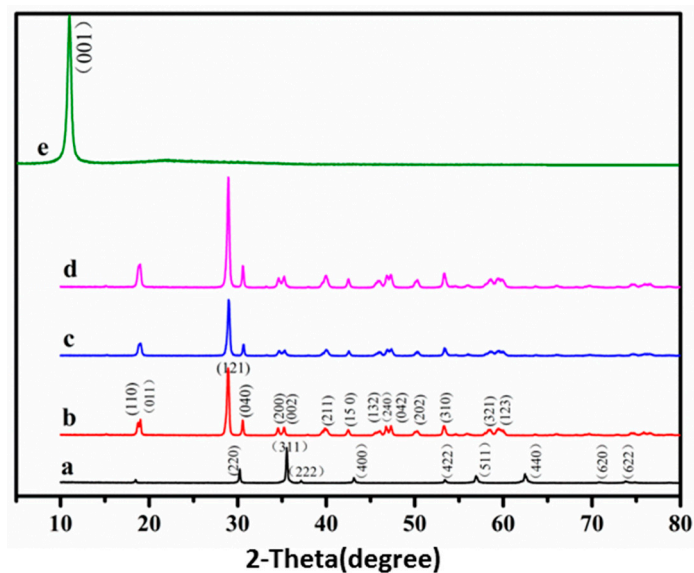
Figure 1. XRD patterns of (**a**) $Mn_{1-x}Zn_xFe_2O_4$; (**b**) $BiVO_4$; (**c**) $BiVO_4/Mn_{1-x}Zn_xFe_2O_4$; (**d**) $BiVO_4/Mn_{1-x}Zn_xFe_2O_4/RGO$ (reduced graphene oxide); (**e**) GO (graphene oxide).
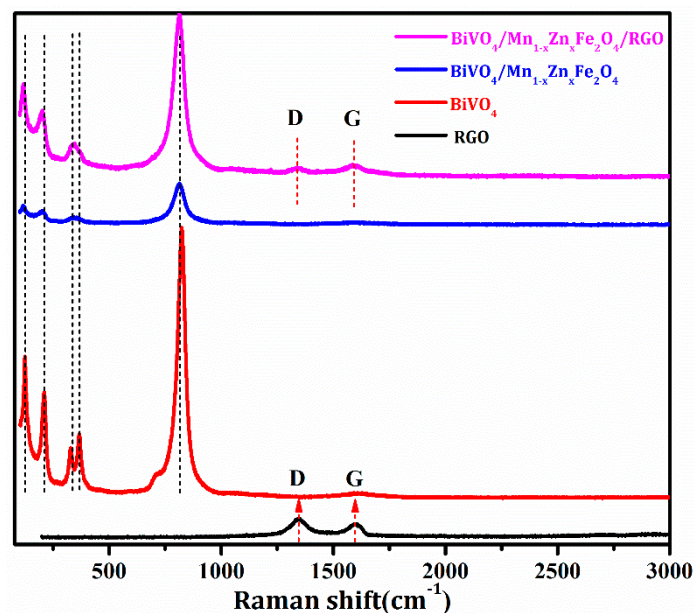
Figure 2. Raman spectra of RGO, $BiVO_4$, $Mn_{1-x}Zn_xFe_2O_4/BiVO_4$, and $Mn_{1-x}Zn_xFe_2O_4/BiVO_4/RGO$.

To investigate the valence state and the surface property of $BiVO_4/Mn_{1-x}Zn_xFe_2O_4/RGO$, XPS spectrum characterization was employed. As displayed in Figure 3a, the spectrum intensity of C 1s in $BiVO_4/Mn_{1-x}Zn_xFe_2O_4/RGO$ was larger than that in $BiVO_4/Mn_{1-x}Zn_xFe_2O_4$, namely, the introduction of RGO brought the intensity increase of C 1s. The spectrum intensity of oxygen-containing functional groups in Figure 3b was larger than that in Figure 3c, meaning

the decrease of GO and the increase of RGO in $BiVO_4/Mn_{1-x}Zn_xFe_2O_4/RGO$ sample. This feature confirmed the efficient reduction of GO and the valence states for various elements in $BiVO_4/Mn_{1-x}Zn_xFe_2O_4/RGO$.

Figure 4 was the transmission electron microscopy (TEM) images of the as-synthesized $BiVO_4/Mn_{1-x}Zn_xFe_2O_4/RGO$. In detail, there were the black core of $Mn_{1-x}Zn_xFe_2O_4$ and the gray shell of $BiVO_4$, and RGO sheets had good interfacial contact with $BiVO_4/Mn_{1-x}Zn_xFe_2O_4$ spherical particle. In other words, there was an overlap between $BiVO_4/Mn_{1-x}Zn_xFe_2O_4$ and RGO. At the same time, energy dispersive spectroscopy (EDS) of the composite revealed the presence of Fe, Bi, V, O, and C elements in $Mn_{1-x}Zn_xFe_2O_4$, $BiVO_4$, and RGO, which was in good agreement with XPS investigation.

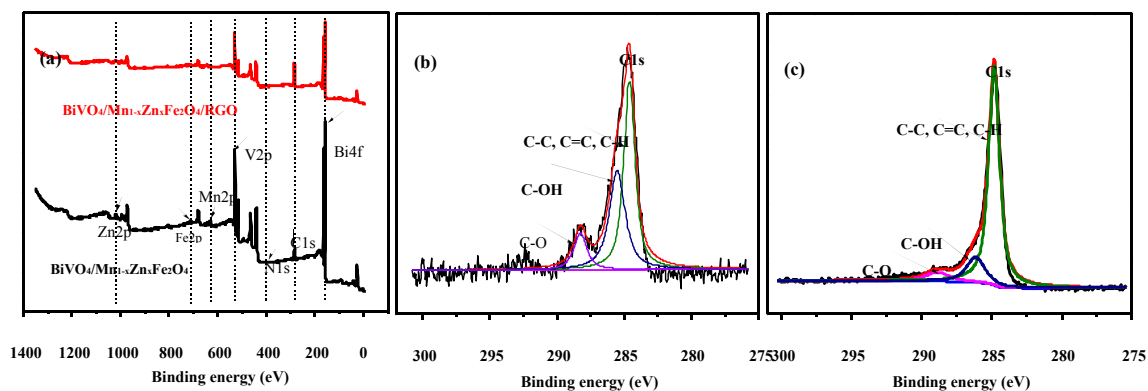**Figure 3.** XPS survey spectra of (**a**) full range scan of $BiVO_4/Mn_{1-x}Zn_xFe_2O_4$ and $BiVO_4/Mn_{1-x}Zn_xFe_2O_4/RGO$; (**b**) C1s peaks in $BiVO_4/Mn_{1-x}Zn_xFe_2O_4$ (**c**) C1s peaks in $BiVO_4/Mn_{1-x}Zn_xFe_2O_4/RGO$.
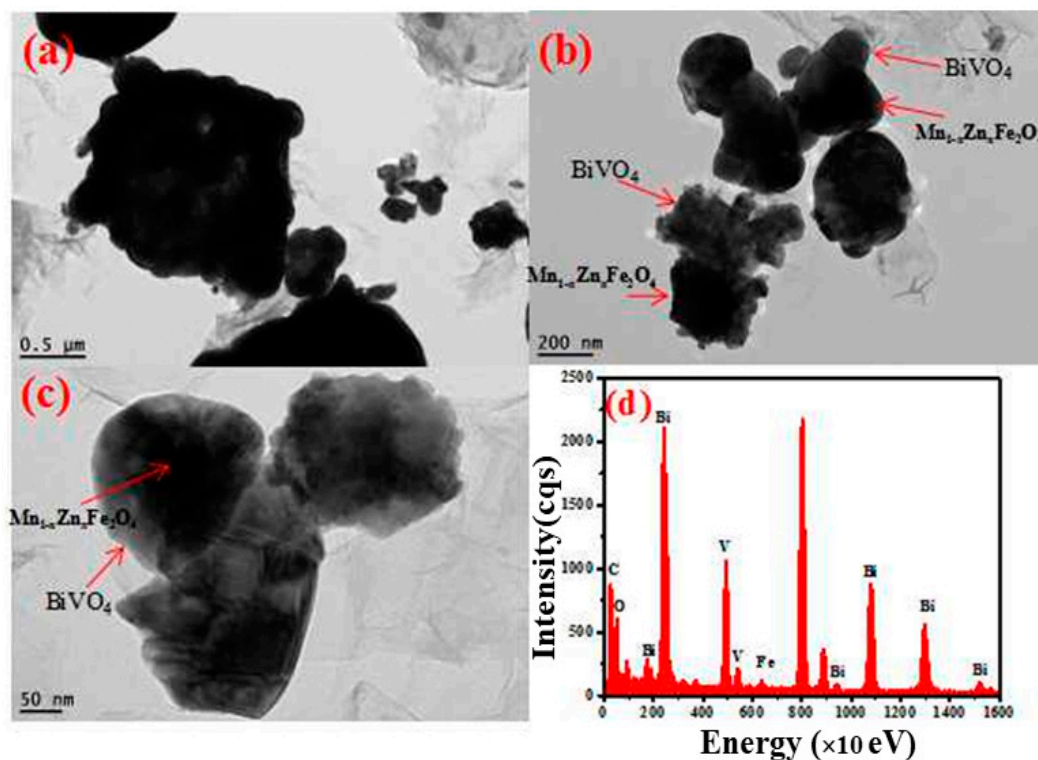
Figure 4. TEM images of $Mn_{1-x}Zn_xFe_2O_4/BiVO_4/RGO$ with different resolution (**a–c**) and (**d**) EDS of $Mn_{1-x}Zn_xFe_2O_4/BiVO_4/RGO$.

Specific surface area of the as-obtained compounds was determined with the adsorption instrument, and the result was shown in Figure 5. The adsorption–desorption isotherms in Figure 5 were the typical isotherm III, agreeing with the reference report [26]. The discrete curve of $BiVO_4/Mn_{1-x}Zn_xFe_2O_4/RGO$ was in p/p_0 range of 0.45–0.55, and the pore diameter distribution was mainly 2–10 nm, and the most probable distribution was located in 4 nm. It was deduced that the introduction of RGO caused the mesopore increase and the macropore decrease. Thus, there was the uniform surface structure in the ternary composite. Calculating with the data in Figure 6, the specific surface area of $BiVO_4/Mn_{1-x}Zn_xFe_2O_4/RGO$ was 8.84 m^2/g, and that of $BiVO_4/Mn_{1-x}Zn_xFe_2O_4$ was only 2.22 m^2/g. The incorporation of RGO enhanced the specific surface area compared with $BiVO4/Mn_{1-x}Zn_xFe_2O_4$. The larger specific surface area provided more active surface sites, more free space to improve the mobility of photo-induced electrons, and further facilitated the effective migration of charge carriers, leading to the remarkable improvement of photocatalytic performance [27]. The surface structure characterization could demonstrate, in advance, the photocatalytic activity of $BiVO_4/Mn_{1-x}Zn_xFe_2O_4/RGO$ to some extent.
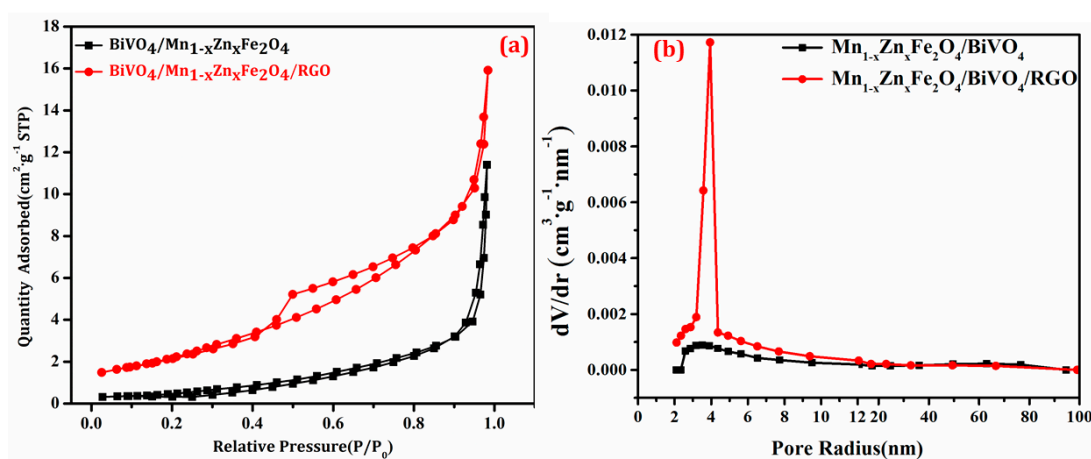

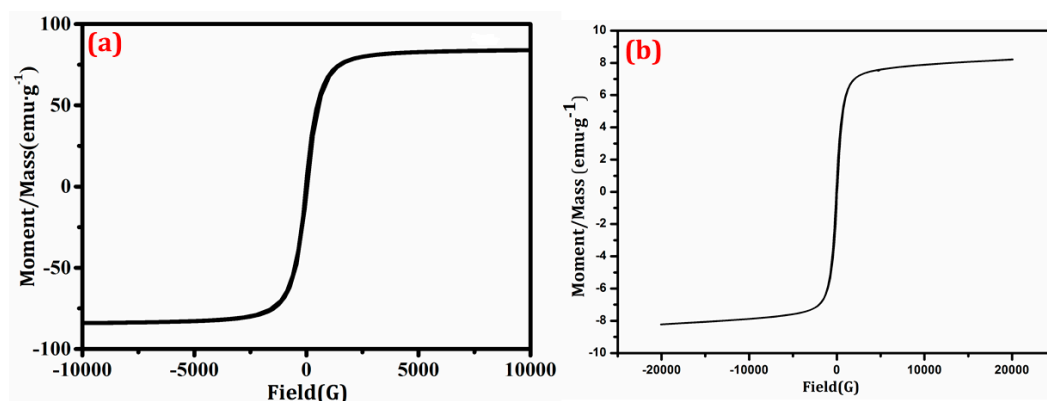**Figure 5.** The adsorption–desorption isotherms of compounds (**a**), and the pore size distribution curves of compounds (**b**).

Figure 6. Hysteresis loops of products (**a**) $Mn_{1-x}Zn_xFe_2O_4$; (**b**) $BiVO_4/Mn_{1-x}Zn_xFe_2O_4/RGO$.

3.3. Magnetic Performance and Optical Properties

The magnetic hysteresis loops of the samples were displayed in Figure 6. The saturation magnetization (Ms) of $Mn_{1-x}Zn_xFe_2O_4$ and $BiVO_4/Mn_{1-x}Zn_xFe_2O_4/RGO$ were 84.03 and 8.21 emu g^{-1}, respectively. Ms of the compounds was lower than that of the pure $Mn_{1-x}Zn_xFe_2O_4$, owing to the amount decrease of the magnetic substance quantity in per unit composite. It was obvious that the prepared composite $BiVO_4/Mn_{1-x}Zn_xFe_2O_4/RGO$ had a soft-magnetic feature like pure

$Mn_{1-x}Zn_xFe_2O_4$, which further confirmed than the synthesized composite must be comprised of $Mn_{1-x}Zn_xFe_2O_4$ component [20,26].

It was worth noting that Ms was no attenuation after $BiVO_4/Mn_{1-x}Zn_xFe_2O_4/RGO$ was employed after five rounds of recycling, indicating the stable magnetism of the as-prepared composite photocatalyst. More importantly, the compound exhibited outstanding paramagnetism because both coercivity (Hc) and remnant magnetization (Mr) were near to zero. Obviously, the excellent magnetic property ensured the high recovery ratio of $BiVO_4/Mn_{1-x}Zn_xFe_2O_4/RGO$ using an external magnet after reaction.

The light absorption ability of the as-prepared samples was investigated with UV–vis DRS, and the diffuse reflectance spectra were recorded in Figure 7. It was seen from Figure 8a that the maximum absorption wavelength (λ_{max}) of pure $BiVO_4$ was about 500 nm. The further insights revealed the absorbance (at λ_{max} = 500 nm) of the compounds was higher than that of $BiVO_4$. The band gap energy (E_g) was estimated from $(Ahv)^{1/2} \sim hv$ plots [5] (Figure 7b). E_g of $BiVO_4$, $BiVO_4/Mn_{1-x}Zn_xFe_2O_4$, and $BiVO_4/Mn_{1-x}Zn_xFe_2O_4/RGO$ were approximately 2.36 eV, 2.36 eV, and 2.27 eV, respectively. The introduction of $Mn_{1-x}Zn_xFe_2O_4$ did not extend the absorbance light range of $BiVO_4$ [20]. However, the introduction of RGO could be conducive to lessen E_g, leading to the enhancement of visible light absorbance for $BiVO_4/Mn_{1-x}Zn_xFe_2O_4$. It is true that the great light absorption was closely related to good photocatalytic activity of catalysts [26].
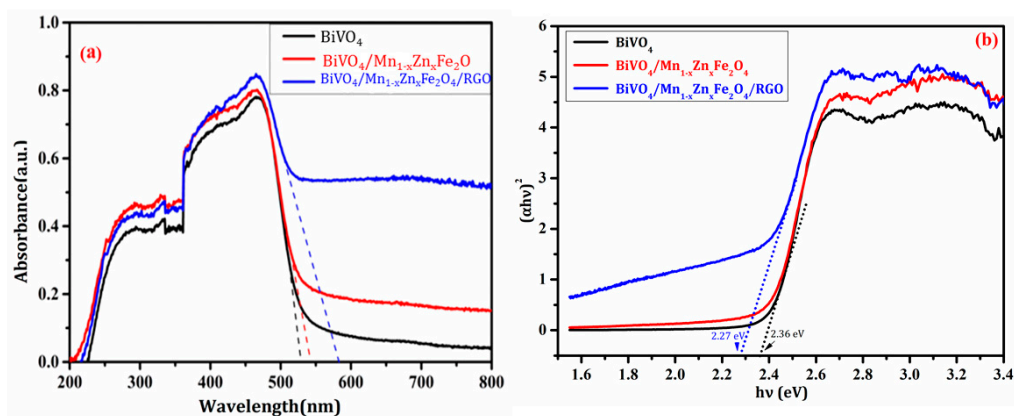

Figure 7. UV–vis diffuse reflectance spectra of the as-prepared products (**a**) and corresponding the plot of $(Ahv)^{1/2}$ versus hv (**b**).
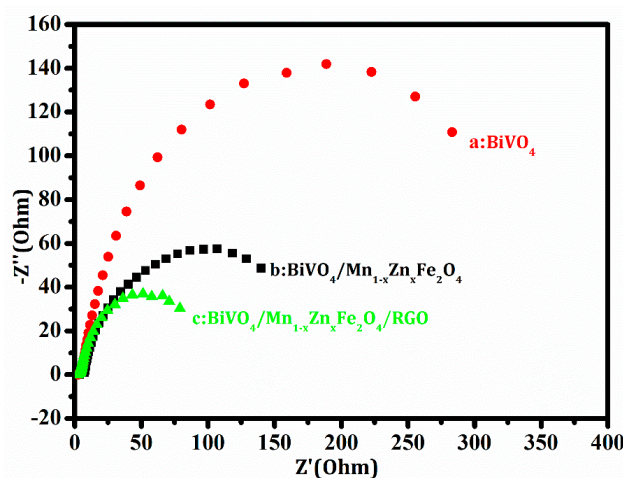

Figure 8. EIS of the work electrode containing $BiVO_4$ (**a**); $BiVO_4/Mn_{1-x}Zn_xFe_2O_4$ (**b**) and $BiVO_4/Mn_{1-x}Zn_xFe_2O_4/RGO$ (**c**).

3.4. Electrochemical Performance

Electrochemical impedance spectroscopy (EIS) was an effective approach to evaluate electron transfer ability in the interface between solid phase electrodes and electrolyte solution [28]. The typical impedance spectra of the samples were displayed with Nyquist plots. The semicircle diameter in Figure 8 became small when RGO inserted in the work electrode contained the compound. This change implied the resistance decrease and the conductivity increase in the test interface. The charge-transfer resistance (R_{ct}) of the samples was gained by fitting the data from Figure 8. R_{ct} of $BiVO_4$, $BiVO_4/Mn_{1-x}Zn_xFe_2O_4$, and $BiVO_4/Mn_{1-x}Zn_xFe_2O_4/RGO$ were 351.0 Ω cm^2, 206.0 Ω cm^2, and 103.0 Ω cm^2, respectively. It was clear that R_{ct} of the ternary composite was the lowest.

The good electron accepting and transporting properties of RGO could contribute to the prevention of charge recombination. It was reasonable that the introduction of RGO was beneficial to the efficient charge separation and transportation in the compound interface. The electrochemical behavior brought high conductivity of the comprising electrode. As a result, the enhancement of conductivity promoted the improvement of photocatalytic activity for $BiVO_4/Mn_{1-x}Zn_xFe_2O_4/RGO$.

3.5. Photocatalytic Activity, Stability, and Corresponding Mechanism

The photocatalytic activity was probed with photodegradation of RhB dye, and the result was shown in Figure 9. It was found from Figure 9 that the degradation ratio of RhB with $BiVO_4/Mn_{1-x}Zn_xFe_2O_4/RGO$ under visible light irradiation reached to 96.0% after only 1.5 h reaction. It is worth noting that the self-degradation of RhB was very weak in the comparative test. It took about 3 h to get the same degradation ratio (96.0%) with pure $BiVO_4$ as well as $BiVO_4/Mn_{1-x}Zn_xFe_2O_4$ under identical conditions. Significantly, $BiVO_4/Mn_{1-x}Zn_xFe_2O_4/RGO$ exhibited more excellent photocatalytic activity than that of $BiVO_4/Mn_{1-x}Zn_xFe_2O_4$. Moreover, the activity of $BiVO_4/Mn_{1-x}Zn_xFe_2O_4/RGO$ was greatly superior to that of $SrFe_{12}O_{19}/BiVO_4$, as well as $BiVO_4/RGO$, in the literature [19,22]. The high photocatalytic property of the as-produced compound $BiVO_4/Mn_{1-x}Zn_xFe_2O_4/RGO$ was explained as follows: the graphene owned two-dimensional π–π conjugate structure was not only a good electron acceptor, but also a good electronic vector. RGO excited electrons in $BiVO_4/Mn_{1-x}Zn_xFe_2O_4$ and prompted the transferring of the conduction band in itself [29]. It was more interesting that the photocatalytic activity of $BiVO_4/Mn_{1-x}Zn_xFe_2O_4/RGO$ was obviously better than that of $Mn_{1-x}Zn_xFe_2O_4/\beta$-$Bi_2O_3$ in previous our group's report [20].
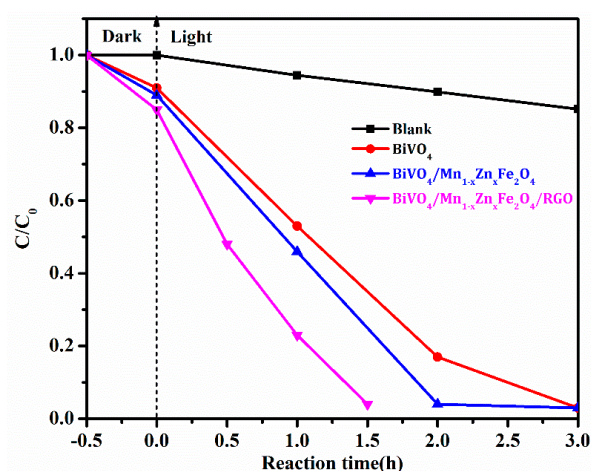

Figure 9. Degradation ratios of rhodamine B (RhB) with photocatalysts.

The stability was a key property in the industrial application of catalytic materials. Each recycling experiment was operated in triplicate, and average values and standard deviations were also shown in Figure 10. The degradation ratio of RhB in the fifth recycling was still 85.0% after 1.5 h of reaction

under the same test parameters. The photocatalytic activity was only reduced a little within five recycles. The result revealed good stability of $BiVO_4/Mn_{1-x}Zn_xFe_2O_4/RGO$.
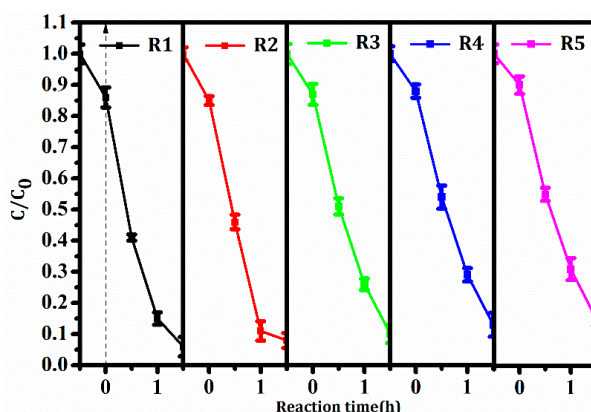
Figure 10. Cycling test of $BiVO_4/Mn_{1-x}Zn_xFe_2O_4/RGO$ in RhB photodegradation (five recycles).

Figure 11 was FTIR spectra of the compounds. The peaks at 473.7 cm^{-1} and 412.4 cm^{-1} in Figure 11a,b were assigned to Zn–O and Fe–O vibrations in $Mn_{1-x}Zn_xFe_2O_4$. Characteristic patterns of V–O symmetric and asymmetric stretching vibrations spectra in $BiVO_4$ were present at 734.3 cm^{-1} and 823.4 cm^{-1}. The abovementioned peak location and intensity of $Mn_{1-x}Zn_xFe_2O_4$ and $BiVO_4$ were not varied, demonstrating a high stability of $BiVO_4/Mn_{1-x}Zn_xFe_2O_4$ during the photocatalytic reaction. The peak at 1625.9 cm^{-1} in Figure 11 belonged to C=C stretch of aromatic group in RGO. The peak at 1629.5 cm^{-1} in Figure 11b was weaker than that in Figure 11a, due to a little loss of RGO quantity after the fifth cycle. The absorption peaks located at around 1400.0 cm^{-1} and 1065.0 cm^{-1} illustrated the functional group of RGO [30]. By comparing pattern (a) and (b) in Figure 11, the typical peaks were detected in the spectra of the fresh, as well as the recovered compound. Thereby, it was concluded that the structure of $BiVO_4/Mn_{1-x}Zn_xFe_2O_4/RGO$ was stable in the process of RhB photocatalytic degradation.
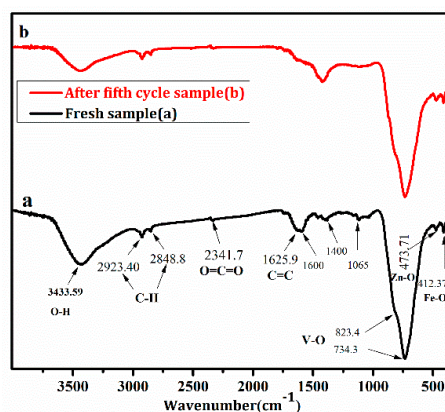
Figure 11. FTIR spectra of $Mn_{1-x}Zn_xFe_2O_4/BiVO_4/RGO$ (**a**) the fresh sample; (**b**) the recovered sample.

The photocatalytic mechanism of $BiVO_4/Mn_{1-x}Zn_xFe_2O_4/RGO$ was probed with radical scavengers [31]. *t*-BuOH (•OH scavenger), EDTA-Na$_2$ (h$^+$ scavenger), and BZQ (•O$_2{}^-$ scavenger) were employed to ascertain the dominant radical species in the photocatalytic degradation of RhB with the as-synthesized compound. Degradation ratios of RhB under these scavengers were given in Figure 12. The photodegradation ratio of RhB was 72.0% and 65.0% only when 5.0 mM *t*-BuOH and

1.0 mM EDTA-Na$_2$ were added into the reaction system. Namely, h$^+$ or ●OH scavenger brought about the decrease of degradation ratios. Thus, the photocatalytic activity of the compound greatly decreased. The inactivation of the photocatalytic test was evidently proven when 1 mM BZQ was added in the same reaction system. The above results demonstrated that the most active species was ●O$_2^-$, though ●OH and h$^+$ also contributed to the photocatalytic activity of BiVO$_4$/Mn$_{1-x}$Zn$_x$Fe$_2$O$_4$/RGO.

　　　Figure 13 described the electron–hole pairs forming process under the light irradiation. The potentials of conduction band (CB) and valence band (VB) of BiVO$_4$ were 0.46 eV and 2.86 eV, respectively (referring to hydrogen electrode, NHE). The electrons in VB were excited to CB under visible light irradiation, forming driven-electrons (e$^-$) and holes (h$^+$). The VB potential of BiVO$_4$ was close to E$^\theta$ of ●OH/H$_2$O, and the CB potential was larger than E$^\theta$ of O$_2$/●O$_2^-$. This meant that electrons were able to directly reduce O$_2$ molecules into superoxide O$_2^-$. Besides, RhB molecules were directly oxidized by the holes on VB of BiVO$_4$. In addition, there were much more active adsorption centers and photocatalytic reaction sites in RGO with a large surface area. These active centers and sites were beneficial to the improvement of the photocatalytic activity. As a good electron acceptor and electronic vector, RGO facilitates the transmission of photo-produced electrons, which was conducive to the separation of photo-produced electrons and holes, and further promoted the formation of ●O$_2^-$. It was ensured that ●O$_2^-$ played the main role for the RhB photodegradation, though ●OH and h$^+$ had a collaborative oxidation role in the photocatalytic reaction of BiVO$_4$/Mn$_{1-x}$Zn$_x$Fe$_2$O$_4$/RGO.
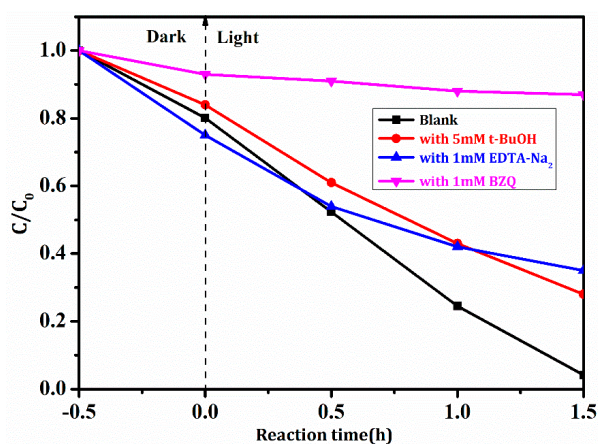
Figure 12. Photodegradation ratios of RhB with BiVO$_4$/Mn$_{1-x}$Zn$_x$Fe$_2$O$_4$/RGO under scavengers.
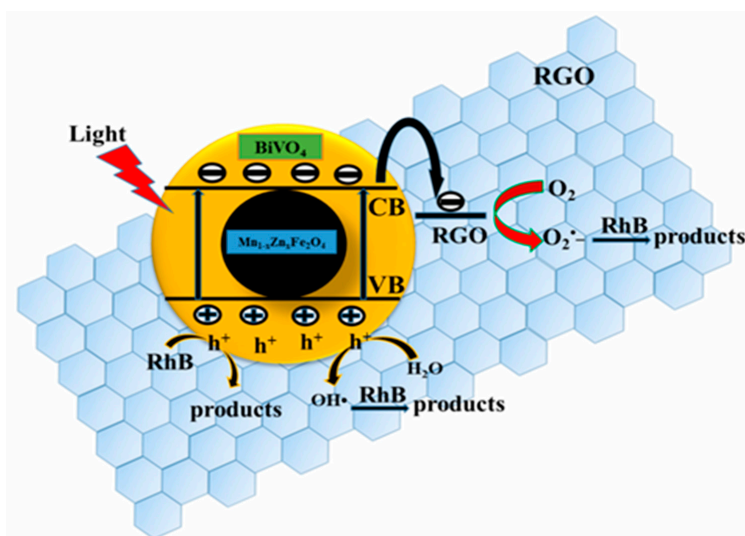
Figure 13. Photocatalytic scheme of BiVO$_4$/Mn$_{1-x}$Zn$_x$Fe$_2$O$_4$/RGO under visible light irradiation.

In fact, since our group found that the magnetic composite $ZnFe_2O_4/SrFe_{12}O_{19}$ had a highly photocatalytic activity in 2013 [27], we firmly thought that the stable magnetic field from $SrFe_{12}O_{19}$ itself could promote the separation of photo-generated electrons and holes, and furthermore, that the photocatalyst could produce more photo-generated electrons and holes under identical light irradiation. Thus, the photoelectric transformation efficiency would be boosted. Our group the studied $BiVO_4/SrFe_{12}O_{19}$, $Bi_2O_3/SrFe_{12}O_{19}$, and $BiOCl/SrFe_{12}O_{19}$ [22,32,33] magnetic heterojunction to confirm previous speculation. However, these studies about its photoelectron transfer mechanism were not enough. In future work, our group will continue to attempt to confirm our speculation via experimental and theoretical calculations. Of course, this work was carried out in order to compare with $SrFe_{12}O_{19}$ functions.

4. Conclusions

Magnetic photocatalyst $BiVO_4/Mn_{1-x}Zn_xFe_2O_4/RGO$ was synthesized with the simple and economical roasting-reduction approach. The photocatalyst exhibited excellent photocatalytic activity and stability. The degradation ratio of RhB reached 96.0% under visible light irradiation after only 1.5 h reaction with the photocatalyst. The degradation ratio of RhB was still maintained at 85.0% after five cycles of photocatalytic reaction. Here, the incorporation of RGO enhanced the specific surface area compared with $BiVO4/Mn_{1-x}Zn_xFe_2O_4$.The larger specific surface area provided more active surface sites, more free space to improve the mobility of photo-induced electrons, and further facilitated the effective migration of charge carriers, leading to the remarkable improvement of photocatalytic performance. RGO was the effective acceptor as well as transporter of photo-generated electron–hole pairs. $\bullet O_2^-$ was the most active species in this photocatalytic reaction. We hope this photocatalyst has a wide application in organic contaminants removal or environmental pollution control in practical.

Author Contributions: Conceptualization, T.X. and T.X.; Methodology, C.L.; Formal Analysis, H.L. and T.X.; Investigation, H.L. and J.Y.; Resources, C.L.; Data Curation, H.L. and T.X.; Writing-Original Draft Preparation, H.L. and T.X.; Writing-Review & Editing, T.X., C.L., and L.X.; Supervision, C.L. and L.X.

Conflicts of Interest: The authors declare that they have no conflict of interest.

References

1. Willkomm, J.; Katherine, L.O.; Reynal, A. Dye-sensitised semiconductors modified with molecular catalysts for light-driven H_2 production. *Chem. Soc. Rev.* **2016**, *45*, 9–23. [CrossRef] [PubMed]
2. Kudo, A.; Ueda, K.; Kato, H.; Mikami, I. Photocatalytic O_2 Evolution under Visible Light Irradiation on $BiVO_4$ in Aqueous $AgNO_3$ Solution. *Catal. Lett.* **1998**, *53*, 229–230. [CrossRef]
3. Zhu, G.Q.; Hojamberdievc, M.; Que, W.X.; Liu, P. Hydrothermal synthesis and visible-light photocatalytic activity of porous peanut-like $BiVO_4$ and $BiVO_4/Fe_3O_4$ submicron structures. *Ceram. Int.* **2013**, *39*, 9163–9172. [CrossRef]
4. Zhang, L.S.; Lian, J.S.; Wu, L.Y.; Duan, Z.R.; Jiang, J.; Zhao, L.J. Synthesis of a Thin-Layer MnO_2 Nanosheet-Coated Fe_3O_4 Nanocomposite as a Magnetically Separable Photocatalyst. *Langmuir* **2014**, *30*, 7006–7013. [CrossRef] [PubMed]
5. Zhang, W.Q.; Wang, M.; Zhao, W.J.; Wang, B.Q. Magnetic composite photocatalyst $ZnFe_2O_4/BiVO_4$: Synthesis, characterization, and visible-light photocatalytic activity. *Dalton Trans.* **2013**, *42*, 15464–15474. [CrossRef] [PubMed]
6. Laohhasurayotin, K.; Pookboonmee, S.; Viboonratanasri, D.; Kangwansupamonkon, W. Preparation of magnetic photocatalyst nanoparticles—$TiO_2/SiO_2/Mn$–Zn ferrite—And its photocatalytic activity influenced by silica interlayer. *Mater. Res. Bull.* **2012**, *47*, 1500–1507. [CrossRef]

7.   Dong, X.L.; Shao, Y.; Zhang, X.X.; Ma, H.C.; Zhang, X.F.; Shi, F.; Ma, C.; Xue, M. Synthesis and properties of magnetically separable $Fe_3O_4/TiO_2/Bi_2O_3$ photocatalysts. *Res. Chem. Intermed.* **2014**, *40*, 2953–2961. [CrossRef]

8.   Ma, P.C.; Jiang, W.; Wang, F.H.; Li, F.S.; Shen, P.; Chen, M.D.; Wang, Y.J.; Liu, J.; Li, P.Y. Synthesis and photocatalytic property of Fe_3O_4@TiO_2 core/shell nanoparticles supported by reduced graphene oxide sheets. *J. Alloys Compd.* **2013**, *578*, 501–506. [CrossRef]

9.   Dong, S.Y.; Cui, Y.R.; Wang, Y.F.; Li, Y.K.; Hu, L.M.; Sun, J.Y.; Sun, J.H. Designing three-dimensional acicular sheaf shaped $BiVO_4$/reduced graphene oxide composites for efficient sunlight-driven photocatalytic degradation of dye wastewater. *Chem. Eng. J.* **2014**, *249*, 102–110. [CrossRef]

10. Gupta, B.; Melvin, A.A.; Matthews, T.; Dhara, S.; Dash, S.; Tyagi, A.K. Facile gamma radiolytic methodology for TiO2-rGO synthesis: Effect on photo-catalytic H_2 evolution. *Int. J. Hydrog. Energy* **2015**, *40*, 5815–5823. [CrossRef]

11. Aiga, N. Electron−Phonon Coupling Dynamics at Oxygen Evolution Sites of Visible-Light-Driven Photocatalyst: Bismuth Vanadate. *J. Phys. Chem. C* **2013**, *117*, 9881–9886. [CrossRef]

12. Boruah, P.K.; Borthakur, P.; Darabdhara, G.; Kamaja, C.K.; Karbhal, I.; Shelke, M.V.; Phukan, P.; Saikiad, D.; Das, M.R. Sunlight assisted degradation of dye molecules and reduction of toxic Cr(VI) in aqueous medium using magnetically recoverable Fe_3O_4/reduced graphene oxide nanocomposite. *RSC Adv.* **2016**, *6*, 11049–11063. [CrossRef]

13. Li, J.Q.; Guo, Z.Y.; Liu, H.; Du, J.; Zhu, Z.F. Two-step hydrothermal process for synthesis of F-doped $BiVO_4$ spheres with enhanced photocatalytic activity. *J. Alloys Compd.* **2013**, *581*, 40–45. [CrossRef]

14. Xu, L.; Huang, W.Q.; Wang, L.L.; Tian, Z.A.; Hu, W.Y.; Ma, Y.M.; Wang, X.; Pan, A.L.; Huang, G.F. Insights into Enhanced Visible-Light Photocatalytic Hydrogen Evolution of g-C_3N_4 and Highly Reduced Graphene Oxide Composite: The Role of Oxygen. *Chem. Mater.* **2015**, *27*, 1612–1621. [CrossRef]

15. Wu, X.F.; Wen, L.L.; Lv, K.L.; Deng, K.J.; Tang, D.G.; Ye, H.P.; Du, D.Y.; Liu, S.L.; Li, M. Fabrication of ZnO/graphene flake-like photocatalyst with enhanced photoreactivity. *Appl. Surf. Sci.* **2015**, *358*, 130–136. [CrossRef]

16. Yang, X.F.; Qin, J.L.; Li, Y.; Zhang, R.X.; Tang, H. Graphene-spindle shaped TiO_2 mesocrystal composites: Facile synthesis and enhanced visible light photocatalytic performance. *J. Hazard. Mater.* **2013**, *261*, 342–350. [CrossRef] [PubMed]

17. Wang, A.L.; Shen, S.; Zhao, Y.B.; Wu, W. Preparation and characterizations of $BiVO_4$/reduced graphene oxide nanocomposites with higher visible light reduction activities. *J. Colloid Interface Sci.* **2015**, *445*, 330–336. [CrossRef] [PubMed]

18. Yan, Y.; Suna, S.F.; Song, Y.; Yan, X.; Guan, W.S.; Liu, X.L.; Shi, W.D. Microwave-assisted in situ synthesis of reduced graphene oxide-$BiVO_4$ composite photocatalysts and their enhanced photocatalytic performance for the degradation of ciprofloxacin. *J. Hazard. Mater.* **2013**, *250–251*, 106–114. [CrossRef] [PubMed]

19. Lia, Y.K.; Dong, S.Y.; Wang, Y.F.; Sun, J.Y.; Li, Y.F.; Pi, Y.Y.; Hu, L.M.; Sun, J.H. Reduced graphene oxide on a dumbbell-shaped $BiVO_4$ photocatalyst for an augmented natural sunlight photocatalytic activity. *J. Mol. Catal. A Chem.* **2014**, *387*, 138–146. [CrossRef]

20. Xie, T.P.; Xu, C.L.L.L.J.; Li, H. New Insights into $Mn_xZn_{1−x}Fe_2O_4$ via Fabricating Magnetic Photocatalyst Material $BiVO_4$/ $Mn_xZn_{1−x}Fe_2O_4$. *Materials* **2018**, *11*, 335. [CrossRef] [PubMed]

21. Liu, C.L.; He, C.L.; Xie, T.P.; Yang, J. Reduction of Graphite Oxide Using Ammonia Solution and Detection Cr(VI) with Graphene-Modified Electrode. *Fuller. Nanotub. Carbon Nanostruct.* **2015**, *23*, 125–130. [CrossRef]

22. Liu, C.L.; Li, H.; Ye, H.P.; Xu, L.J. Preparation and Visible-Light-Driven Photocatalytic Performance of Magnetic $SrFe_{12}O_{19}/BiVO_4$. *J. Mater. Eng. Perform.* **2015**, *24*, 771–777.

23. Cui, H.Y.; Yang, X.F.; Gao, Q.X. Facile synthesis of grapheme oxide-enwrapped Ag_3PO_4 composites with highly efficient visible light photocatalytic performance. *Mater. Lett.* **2013**, *93*, 28–31. [CrossRef]

24. Fu, Y.S.; Sun, X.Q.; Wang, X. $BiVO_4$–graphene catalyst and its high photocatalytic performance under visible light irradiation. *Mater. Chem. Phys.* **2011**, *131*, 325–330. [CrossRef]

25. Yu, Q.Q.; Tang, Z.R.; Xu, Y.J. Synthesis of $BiVO_4$ nanosheets-graphene composites toward improved visible light photoactivity. *J. Energy Chem.* **2015**, *23*, 564–574. [CrossRef]

26. Xie, T.P.; Xu, L.J.; Liu, C.L.; Wang, Y. Magnetic composite $ZnFe_2O_4/SrFe_{12}O_{19}$: Preparation, characterization, and photocatalytic activity under visible light. *Appl. Surf. Sci.* **2013**, *273*, 684–691. [CrossRef]

Nanomaterials **2018**, *8*, 380

13 of 13

27. Wang, B.; Ru, Q.; Su, C.Q.; Cheng, S.K.; Liu, P.; Guo, Q.; Hou, X.H.; Su, S.C.; Ling, C.C. $Ni_{12}P_5$ Nanoparticles Hinged by Carbon Nanotubes as 3D Mesoporous Anodes for Lithium-Ion Batteries. *ChemElectroChem* **2018**. [CrossRef]
28. Sun, L.L.; Wu, X.L.; Meng, M.; Zhu, X.B.; Chu, P.K. Enhanced Photodegradation of Methyl Orange Synergistically by Microcrystal Facet Cutting and Flexible Electrically-Conducting Channels. *J. Phys. Chem. C* **2014**, *118*, 28063–28068. [CrossRef]
29. Zhang, H.; Lv, X.J.; Li, Y.M.; Wang, Y.; Li, J.H. P25-Graphene Composite as a High Performance Photocatalyst. *J. Am. Chem. Soc.* **2010**, *4*, 380–386. [CrossRef] [PubMed]
30. Yang, X.; Chen, W.; Huang, J.; Zhou, Y.; Zhu, Y.; Li, C. Sonochemical synthesis of nanocrystallite Bi_2O_3 as a visible-light-driven photocatalyst. *Sci. Rep.* **2015**, *5*, 10632–10641. [CrossRef] [PubMed]
31. Chen, X.J.; Dai, Y.Z.; Wang, X.Y.; Guo, J.; Liu, T.H.; Li, F.F. Synthesis and characterization of Ag_3PO_4 immobilized with graphene oxide (GO) for enhanced photocatalytic activity and stability over 2,4-dichlorophenol under visible light irradiation. *J. Hazard. Mater.* **2015**, *292*, 9–18. [CrossRef] [PubMed]
32. Xie, T.P.; Liu, C.L.; Xu, L.J.; Yang, J.; Zhou, W. Novel Heterojunction $Bi_2O_3/SrFe_{12}O_{19}$ Magnetic Photocatalyst with Highly Enhanced Photocatalytic Activity. *J. Phys. Chem. C* **2013**, *117*, 24601–24610. [CrossRef]
33. Xie, T.P.; Xu, L.J.; Liu, C.L.; Yang, J.; Wang, M. Magnetic composite $BiOCl–SrFe_{12}O_{19}$: A novel p-n type heterojunction with enhanced photocatalytic activity. *Dalton Trans.* **2014**, *43*, 2211–2220. [CrossRef] [PubMed]